Optics Communications 482 (2021) 126614

Contents lists available at ScienceDirect

Optics Communications

journal homepage: www.elsevier.com/locate/optcom

Mode-resolved analysis of a planar multi-layer plasmonic nanolaser

Zihad Azad [a], Md. Shofiqul Islam [b], Muhammad Anisuzzaman Talukder [a,*]

[a] Department of Electrical and Electronic Engineering, Bangladesh University of Engineering and Technology, Dhaka 1205, Bangladesh
[b] Department of Electrical and Computer Engineering, Faculty of Engineering, King Abdulaziz University, PO Box 80204, Jeddah 21589, Saudi Arabia

ARTICLE INFO

Keywords:
Plasmonic nanolaser
4-level 2-electron model
Photonic crystals
IR-140 dye molecules

ABSTRACT

Plasmonic nanolasers (PNLs) have attracted much attention in recent years due to their light-trapping capabilities beyond the diffraction limit. However, the physics that underpins the lasing action in such devices has not received sufficient treatment in the literature. The contribution of plasmons in PNLs needs to be understood at a granular level for designing enhanced nanoscopic lasers. In this work, we present a modal decomposition-based analysis of a planar PNL that employs a two-dimensional metallic nanohole array interfaced with the gain medium. Using state-of-the-art simulation techniques, we isolate the plasmonic mode that emerges at the metal–gain medium interface interlaced with scattering modes. We present a step-by-step dispersion analysis to identify the possible modes supported by the planar PNL structure and locate the operating point of the PNL. Furthermore, we show how the plasmonic mode regulates the lasing action, and hence, can serve as a tool for laser tunability.

1. Introduction

Lasers are spatiotemporally coherent sources of light that offer competitive applications in a wide range of industries, running the gamut from consumer technology to nuclear fusion [1,2]. However, in many potential sectors, e.g., laser surgery, on-chip optical computing, bio-sensing, and data storage, a compact laser with nanoscale dimensions has become a dire necessity [3]. Unfortunately, conventional microcavity-based lasers are diffraction-limited, i.e., the cavity dimensions cannot be smaller than half of the operating wavelength along any one direction [4]. To overcome this intrinsic limitation, novel mechanisms are being explored to compress electromagnetic energy within subwavelength dimensions [5]. One such crucial avenue of research is the introduction of metal in laser design to induce surface plasmons.

Plasmonic modes – excited in the presence of metallic structures – couple energy way beyond the diffraction limit. Furthermore, the amplificatory characteristic of plasmons can mimic resonator effects [6]. Hence, plasmonic modes have emerged as a promising candidate for designing nanoscale lasers. The first proof-of-principle of a PNL was demonstrated in 2007 [7]. Since then, research interest in this field has witnessed a sharp rise. However, the inclusion of plasmons in laser systems comes with additional ohmic losses in the metal layer [8]. Researchers have implemented heterodox strategies to exploit the many strands of plasmons, as well as to circumvent additional losses such as ohmic losses due to the inclusion of metal. From design point-of-view, PNLs can be divided in the following broad categories: (1) metallic nanowire-based PNLs, (2) metallic nanoparticle-based PNLs, and (3) metallic planar structure-based PNLs. In metallic nanowire-based PNLs, a semiconductor nanowire sits atop a metal layer, and the nanowire is often separated from the metal layer by a nanoscale-thick insulator [9]. In this design, surface plasmon polaritons (SPPs) are hybridized with photonic or waveguide modes, which allows SPPs to traverse longer distances with strong modal confinement [10,11].

In metallic nanoparticle-based PNLs, on the other hand, a fundamental variant of plasmonic mode dubbed localized surface plasmon (LSP) – stationary plasmonic excitation in metallic nanoparticles – is exploited to generate lasing [12–14]. Finally, in planar interfaced PNLs, where layers of different materials are stacked one after another, plasmonic modes that emerge at the interfaces between metal and dielectric materials hybridize with photonic modes [4]. Plane parallel slabbing strategy for designing nanoscale lasers has gained significant interest in PNL research due to its ability to produce higher optical output power compared to the other approaches. Planar interfaced PNLs can come in variants with metallic nanostructures in the interface between metal and dielectric layers for better exploitation of both plasmonic and photonic modes [14]. Recently, a novel structure has been proposed in which a metallic nanohole array (NHA) is used with a nanoscale gain medium for enhanced directionality and efficiency [15]. A one-dimensional photonic crystal (1-D PhC) superposed on the gain medium of the nanolaser of Ref. [15] helps to induce the coupling of stimulated emission energy to optical Tamm plasmon polaritons (TPPs) at the interface between the metal layer and the 1-D PhC [16]. The periodic

* Corresponding author.
E-mail address: anis@eee.buet.ac.bd (M.A. Talukder).

https://doi.org/10.1016/j.optcom.2020.126614
Received 21 September 2020; Received in revised form 8 November 2020; Accepted 11 November 2020
Available online 16 November 2020

nanoholes in NHA couple the TPP mode to free-space, radiative mode via extraordinary optical transmission (EOT). Planar structures have also been shown to induce whispering-gallery modes in PNLs [17,18].

Although there has been significant progress in PNL research, a comprehensive theoretical study of the physics underpinning the lasing action in plasmon-integrated systems is still lacking. Presumably, plasmons are the key mechanism of a PNL. However, due to the diversity of approaches involved, different modes may accompany the fundamental plasmonic mode in different designs. The spectral purity of the output emission, tuning of emission wavelength, and far-field directionality will critically depend on the modes excited within the PNL cavity. Additionally, to understand the lasing mechanism so that improved and novel PNLs can be designed and tailored for various applications, an analysis that decomposes lasing light into constituent modes that resonate inside the nanolaser cavity and make the emission profile will be immensely helpful.

In this work, we carry out a mode-resolved analysis of PNLs that exploit parallel plane interfacing of metal and dielectric media. In particular, we analyze the PNL structure presented in Ref. [15] that has a metallic NHA interfaced with the gain medium so that SPPs evolve at the planar metal–gain medium interface and coalesce at the output as a radiative and spectrally coherent EOT mode. The PNL structure proposed in Ref. [15] effectively separates the lasing emission from the pump pulse, increases the emission intensity, and makes the far-field pattern directional. The internal physics of the proposed parallel plane PNL structure with a metallic NHA was not investigated in Ref. [15] and remained mostly elusive. It was assumed that the plasmonic excitation plays a significant role in the designed PNL structure; however, a definitive link was not explored, let alone established. Additionally, in the research work published in Ref. [15], we found that a few aspects of such plasmonic lasers contradict the conventional physics of laser dynamics. We explained a few things intuitively in Ref. [15]; however, an in-depth analysis with theoretical modeling and computational work that unearths the underlying physics is crucially important for designing improved plasmonic lasers with enhanced and tailored performances.

In this work, we decompose the emission spectra at the output and the resonating modes inside the cavity using state-of-the-art simulation techniques. We calculate the dispersion relations to identify all modes that are supported by the studied PNL structure and find out the operating point of the laser—the point of overlap between the supported modes and the gain bandwidth. We show how we can exploit the SPP mode to tune the lasing spectra. By demonstrating that the gain resonance excites plasmons and the lasing mode shifts in response to the plasmonic mode, we have found a definitive link between the excitation of plasmons and the lasing action of the studied PNL, which may serve as a first-principles framework for understanding and designing future PNLs.

2. Nanolaser structure

We investigate the PNL structure that was presented and discussed in Ref. [15]. In Fig. 1(a), we show a schematic diagram of the structure. A polyurethane (PU) layer spin-coated with fluorescent IR-140 dye molecules that functions as the active medium is placed on the top of a gold layer. IR-140 dye molecules have a broad fluorescence spectrum [19] that makes them a suitable candidate for laser gain medium, especially in widely tunable lasers. Additionally, IR-140 molecules show a superior photo-physical performance when they are used as an active dopant with polymers, as compared to other familiar dye molecules such as Rhodamine 6G or pyrromethene 567 [20]. On the other hand, the use of gold as the metal layer is favored over silver and copper. While copper is not a suitable metal for their inability to excite SPP modes in the near-infrared regime and huge loss incurred within copper, both gold and silver help excite strong SPP modes in the near-infrared regime and support long propagation length for SPP modes with a relatively less loss [21]. However, silver shows a relatively poor performance in comparison with gold due to a lack of chemical stability of silver, susceptibility to surface impurities, and difficulty to grow single-crystalline silver layers [22]. The gold layer is perforated with two-dimensional (2-D) square holes with subwavelength periodicity. The 1-D PhC consisting of 5 pairs of alternating TiO_2 and MgF_2 layers is separated from the gain medium by a comparatively thicker spacer layer of TiO_2. The alternating TiO_2 and MgF_2 layer thicknesses are 108 nm and 165 nm, respectively. The spacer layer thickness is 200 nm, while the IR-140-doped PU gain layer is 325-nm thick. The metal layer has a thickness of 100 nm with 170 nm × 170 nm nanoholes that have a periodicity of 350 nm in both the x- and y-directions. The refractive indices of different dielectric materials used in the PNL structure are provided in Table 1 [15].

Table 1
Refractive indices of dielectric layers.

Material	Refractive Index
TiO_2	2.23
MgF_2	1.38
PU	1.52

The PNL structure is uniformly optically pumped from the PhC side by a normally incident, ultra-short 40 fs plane wave pulse, centered at 800 nm. We set the source intensity to 8.8 $\mu W/cm^2$. The 1-D PhC serves as a distributed Bragg reflector (DBR) to suppress the forward scattering of the pump pulse. The layer thicknesses, as well as refractive indices, are chosen in such a way that the reflectance bandgap of the DBR coincides with the spectrum of pump pulse centered at 790 nm [23]. Fig. 1(b) presents the cross-sectional view of the structure in the x-z plane. SPPs are excited in the metal–gain medium interface, while EOT occurs through the holes in the metal layer to create the lasing emission. In effect, the square holes in the metal layer emit spherical wavefronts that interfere constructively in the far-field to produce a highly directional laser beam.

3. Theoretical modeling and simulation methodology

Theoretical modeling is crucially important in understanding the physics of plasmonic lasing at nanoscopic dimensions and designing improved plasmonic lasers with enhanced performances. Intuitively, the gain resonance from the active medium would transfer excitonic energy to the surface plasmons that act as nanoresonators. However, if a definite causative link between the induced plasmonic mode and the radiative mode in a planar interfaced PNL can be established via theoretical modeling and numerical approach, as pursued in this work, future research works in this field can be carried out in a scientifically more rigorous way.

3.1. Active medium

The absorption of an incident pump signal by IR-140 dye molecules and subsequent fluorescence can be modeled using a 4-level 2-electron system [24]. Effectively, we will analyze the cavity dynamics in a semi-classical framework, where the active medium follows a quantum mechanical description; however, the electromagnetic field propagation follows classical Maxwell's equations. A simplified schematic illustration of the 4-level system is shown in Fig. 2. The incident pump beam excites electrons from the lowest energy level $|0\rangle$ to the highest energy level $|3\rangle$. The excited electrons at level $|3\rangle$ scatter to level $|2\rangle$ via non-radiative decay at a fast rate. The non-radiative decay rate from level $|2\rangle$ to $|1\rangle$ is slow, while the spontaneous radiative transitions from level $|2\rangle$ to $|1\rangle$ lead to lasing emission. The relaxation of electrons from level $|1\rangle$ to $|0\rangle$ is also fast and non-radiative. The relative differences of the decay rates between energy levels lead to the build-up of population density in level $|2\rangle$, and eventually, create population

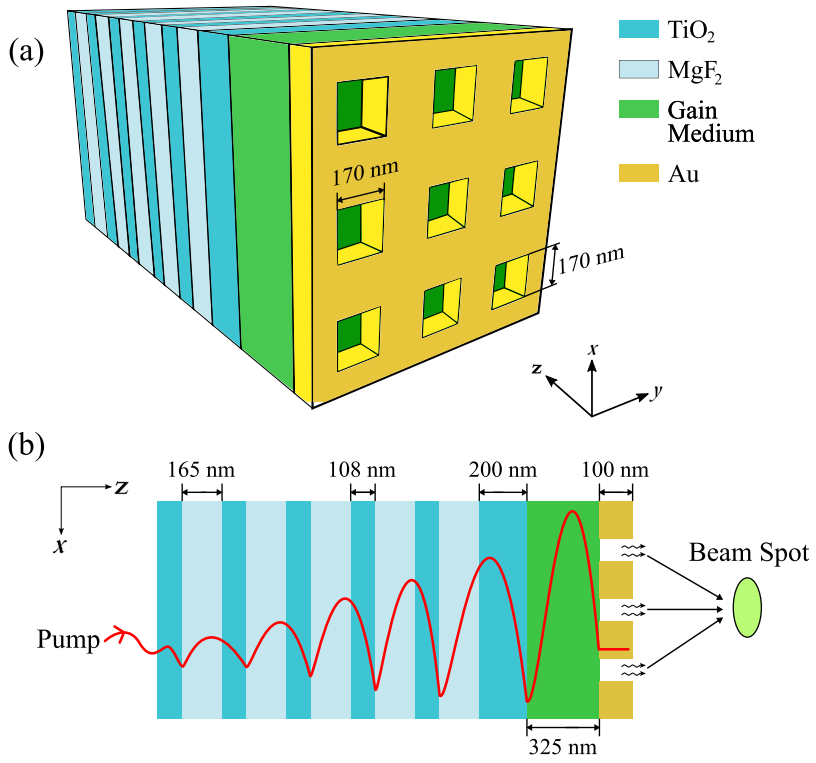

Fig. 1. (a) Perspective view of the studied PNL structure [15]. Alternating layers of TiO_2 and MgF_2 form the 1-D photonic crystal. (b) Cross-sectional view of the PNL structure in the x-z plane.

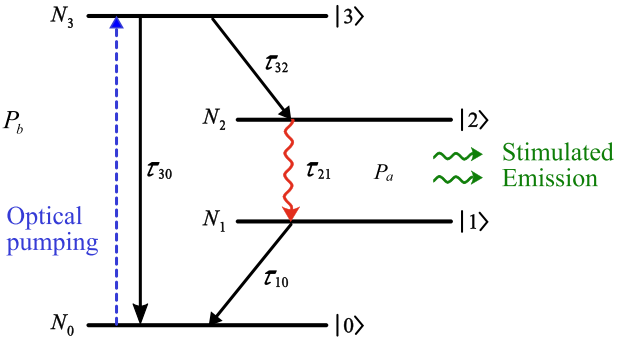

Fig. 2. Schematic diagram of a 4-level 2-electron system.

Table 2
Parameter values for IR-140 dye molecules.

Parameter	Value
Emission wavelength (λ_a)	870 nm
Emission linewidth ($\Delta\lambda_a$)	100 nm
Absorption wavelength (λ_b)	800 nm
Absorption linewidth ($\Delta\lambda_b$)	100 nm
Dye concentration (N_{density})	2×10^{24} cm^{-3}
Polarization decay rate ($\gamma_a=\gamma_b$)	3.9×10^{13} s^{-1}
Radiative decay rate (γ_{rad})	7.2×10^{7} s^{-1}
Transition lifetimes ($\tau_{21}=\tau_{30}$)	1 ns
Transition lifetimes ($\tau_{32}=\tau_{10}$)	10 fs

inversion between levels $|1\rangle$ and $|2\rangle$, which is the elemental condition of lasing action.

In this modeling approach, the two radiative transitions between levels $|2\rangle$ and $|1\rangle$ and between levels $|0\rangle$ and $|3\rangle$ are modeled as two coupled dipole oscillators with polarizations P_a and P_b, respectively. The decay or dephasing rates of P_a and P_b are γ_a and γ_b, respectively.

The governing equations for the coupled dipole oscillators are [25]

$$\frac{d^2\vec{P_a}}{dt^2}+\gamma_a\frac{d\vec{P_a}}{dt}+\omega_a^2\vec{P_a}=\frac{6\pi\varepsilon_0c^3}{\omega_a\tau_{21}}(N_2-N_1)\vec{E}, \tag{1a}$$

$$\frac{d^2\vec{P_b}}{dt^2}+\gamma_b\frac{d\vec{P_b}}{dt}+\omega_b^2\vec{P_b}=\frac{6\pi\varepsilon_0c^3}{\omega_b\tau_{30}}(N_3-N_0)\vec{E}, \tag{1b}$$

where N_i is the normalized population density of level i; ω_a and ω_b are the resonant frequencies of P_a and P_b, respectively; τ_{ij} is the decay time constant between levels i and j; and ε_0 and c are the permittivity and the speed of light in vacuum, respectively. The assumption of two coupled dipole oscillators leads to the following set of equations that regulates the population dynamics among the four energy levels [25]

$$\frac{dN_3}{dt}=-\frac{N_3(1-N_2)}{\tau_{32}}-\frac{N_3(1-N_0)}{\tau_{30}}+\frac{1}{\hbar\omega_b}\vec{E}\cdot\frac{d\vec{P_b}}{dt}, \tag{2a}$$

$$\frac{dN_2}{dt}=\frac{N_3(1-N_2)}{\tau_{32}}-\frac{N_2(1-N_1)}{\tau_{21}}+\frac{1}{\hbar\omega_a}\vec{E}\cdot\frac{d\vec{P_a}}{dt}, \tag{2b}$$

$$\frac{dN_1}{dt}=\frac{N_2(1-N_1)}{\tau_{21}}-\frac{N_1(1-N_0)}{\tau_{10}}-\frac{1}{\hbar\omega_a}\vec{E}\cdot\frac{d\vec{P_a}}{dt}, \tag{2c}$$

$$\frac{dN_0}{dt}=\frac{N_3(1-N_0)}{\tau_{30}}+\frac{N_1(1-N_0)}{\tau_{10}}-\frac{1}{\hbar\omega_b}\vec{E}\cdot\frac{d\vec{P_b}}{dt}. \tag{2d}$$

The model links Eqs. (1) and (2) to the Maxwell–Ampere law given by [25]

$$\frac{d\vec{E}}{dt}=\frac{1}{\varepsilon}\nabla\times\vec{H}-\frac{1}{\varepsilon}N_{\text{density}}\left(\frac{d\vec{P_a}}{dt}+\frac{d\vec{P_b}}{dt}\right), \tag{3}$$

where $\vec{E}$ and $\vec{H}$ are the electric and magnetic fields, respectively, and ε is the permittivity of the background material. Eqs. (1)–(3) form a self-consistent set of equations that are solved by the finite-difference time-domain (FDTD) numerical technique to find out the time-resolved population evolution of the four quantum levels. In this work, we solve Eqs. (1)–(3) using a full-field vectorial three-dimensional (3-D) FDTD

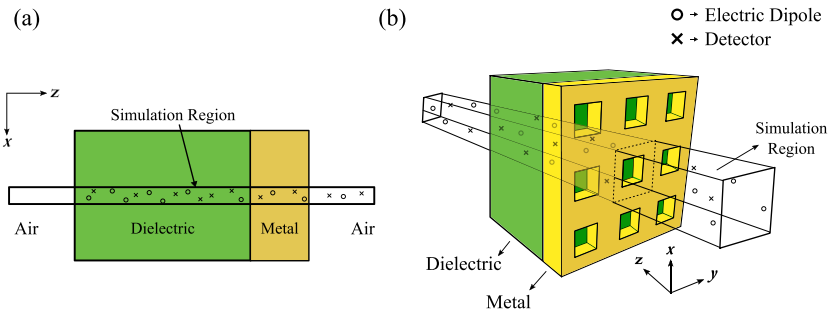

Fig. 3. (a) A thin strip of the metal–dielectric interface along the *x*-*z* plane is included in the simulation region for dispersion analysis. Inside the strip, a number of electric dipoles (marked as circles) is positioned randomly to excite all possible modes of the structure. In a similar fashion, time-domain detectors (marked as crosses) are dispersed across the span of the simulation region to collect field data over time. (b) Same methodology extended to a 3D simulation to record the effect of the metallic NHA on the dispersion of the structure.

technique. We solve a unit cell of the PNL structure in the *x*-*y* plane with Bloch boundary conditions (BCs) applied at the boundaries in the *x*- and *y*-directions. The simulation region in the *z*-direction is 6-μm long that contains all layer thicknesses, air medium on both ends of the structure, the source in the PhC side and a detection plane away from metal layer in the air to record the emission profile. We use perfectly matched layers (PMLs) at the simulation boundaries in the *z*-direction. The pump position is 0.6 μm away from the edge of the PhC structure and the emission is collected at 1 μm away from the metal layer. We use 10-nm mesh sizes in all three directions for the simulation domain except for a small region encompassing the metal layer that has a mesh size of 3.5 nm. We have simulated with even smaller mesh sizes, however, the results do not vary. Typical parameter values used to model the gain medium are derived from Ref. [15] and are given in Table 2.

3.2. Gain lineshape

We calculate the gain coefficient of the IR-140 doped PU material using the well-known expression [26]

$$\alpha_m(\omega) = \frac{\omega_a}{2c}\frac{\chi_0''}{1+[2(\omega-\omega_a)/\Delta\omega_a]^2}, \tag{4}$$

where $\chi_0'' = 3\Delta N\lambda_a^3\gamma_{\text{rad}}/(4\pi^2\Delta\omega_a)$ is the midband value of resonant susceptibility due to transition of excited electrons from level $|2\rangle$ to $|1\rangle$, ω_a is the midband lasing frequency that depends on the energy difference between levels $|2\rangle$ and $|1\rangle$, ΔN is the quantum population difference between levels $|2\rangle$ and $|1\rangle$, γ_{rad} is the radiative decay rate of excited electrons from level $|2\rangle$ to $|1\rangle$, $\Delta\omega_a = \gamma_{\text{rad}} + 1/\tau_{21} + 2\gamma_a$ is the frequency linewidth, and λ_a is the lasing wavelength. Different parameter values used to calculate the gain lineshape of IR-140 embedded in PU are presented in Table 2 [19,27].

3.3. Calculation of dispersion relations

Dispersion diagram – a graphical representation of the relationship between frequency and wavevector – is a powerful analytical tool which reveals the resonant modes of a structure. The key feature of a surface plasmon-based laser is that the gain resonance transfers excitation energy to the plasmons propagating along the metal–dielectric interface. These plasmons, in turn, provide the necessary optical feedback required for lasing action. A dispersion diagram presents a natural tool for our theoretical investigation, in that it would surely encapsulate the information stated above by showing the overlap between the fluorescence bandwidth of the active molecules and the supported modes of the structure, including the surface plasmon resonance (SPR). The spectral overlap between the fluorescence bandwidth and the supported modes essentially represents the laser operating point.

To calculate the dispersion relation, a thin strip of the structure that contains a unit cell with the interfaces is required. If a structure is invariant in one of the directions, e.g., in the *y*-direction, as shown in Fig. 3(a), a 2-D strip in the *x*-*z* plane can be simulated to calculate the dispersion diagram. In 2-D simulations, PMLs are used at the simulation boundaries in the *z*-direction, which allows for the absorption of both propagating and evanescent light waves with minimal reflection [28]. On the other hand, Bloch BC is imposed in the *x*-direction to include the periodicity of the structure in the simulation [29]. Each simulation will yield an allowed band of frequencies for a particular Bloch vector k_x. Extrapolating the aforementioned strategy, we adopt a similar methodology for a 3-D simulation to register the effects of a metallic interface perforated with periodic subwavelength holes, as shown in Fig. 3(b). In 3-D simulations, we use Bloch BCs in the *x*- and *y*-directions, while PML BC in the *z*-direction.

Within the simulation region, a cloud of randomly oriented dipole sources is placed to excite all possible modes that can resonate within the structure. In this work, we use 10 dipoles in the nanoscale-thick simulation region so that multiple dipoles are placed within each of metal, dielectric, and air medium. Therefore, even if a randomly placed dipole is located at the node of a mode, others can still excite the supported modes so that not a single frequency of light that can be supported by the structure is missed out. Correspondingly, 10 time-domain detectors are dispersed over the expanse of the simulation window to collect field data over time. The optical modes that are not supported by the structure would decay away quickly. The supported modes, however, would resonate and be captured by the time-domain detectors. The collected time-domain data are then Fourier-transformed and summed to find out the frequency-domain response (S) of the structure as [30]

$$S = \left|\sum_{i=1}^{M}\sum_{c=x,y,z}\mathcal{F}(E_{i,c}[t])\right|^2, \tag{5}$$

where $E_{i,c}$ is the cth spatial component of the electric field from the ith time-domain detector, $c = x, y, z$ is the x, y and z-component of the field, respectively, and M is the number of time-domain detectors. To calculate the dispersion relation, we run a series of simulations by varying k_x over a large range from zero to 5×10^7 m^{-1}. The collected spectrum data are visualized on a logarithmic scale.

3.4. Spectral isolation of the plasmonic mode

Isolating the contribution of the plasmonic mode is crucially important to identify the feedback mechanism that underpins lasing action in a PNL. To isolate the plasmonic mode, we use a special kind of optical source called total field scattered field (TFSF) source [31]. The TFSF source that we employ has the same properties of the pump beam. The TFSF source emits planar wavefronts and is integrated with a rectangular hollow box known as the "Huygens surface" [32], as shown in Fig. 4. The Huygens surface splits the computation domain, which contains one periodic cell of the PNL structure, into two regions. The

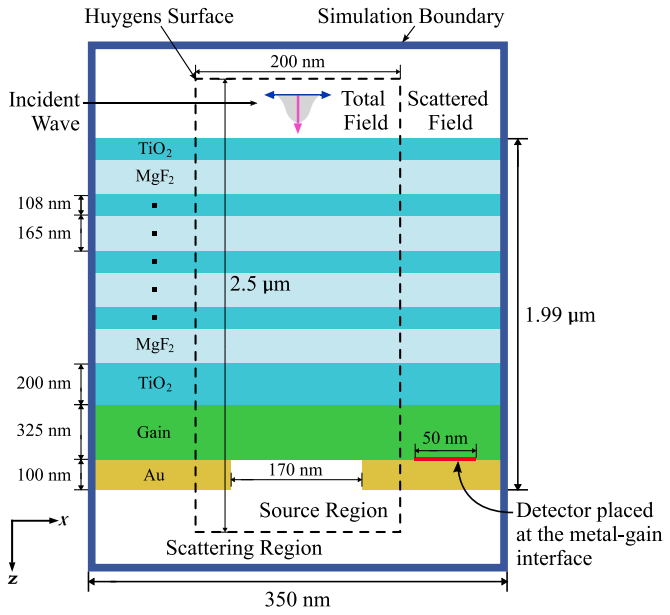

Fig. 4. 2-D schematic illustration of TFSF source. The Huygens surface divides the simulation window into source and scattering regions. A 50 nm × 50 nm 2-D frequency domain detector is placed along the metal–gain interface in the scattering region to record the effect of plasmons.

space confined within the borders of the box is called the source region since it includes the plane wave source. The rest of the simulation region, which falls beyond the borders, is called the scattering region. Inside the box, both incident and scattered fields are present. However, on the outside, only scattered fields are present. The scattered field is obtained by subtracting at the Huygens interfaces any light that is directly transmitted through the source region or reflected from a flat substrate. Since plasmons induced by stimulated emission falls under neither category, they are plentiful in the scattering region. Hence, a 2-D frequency-domain detector is placed at the Au–gain medium interface in the scattering region to record the spectral effect of plasmons. The dimensions of the detector are arbitrary so long as the detector is located in the scattering region and along the Au–gain interface. In this case, we have chosen a 50 nm × 50 nm detector. However, we note that the holes in the metal would act as scattering objects, and their contribution would come interlaced with that of the SPP mode.

4. Results and discussion

4.1. Dispersion analysis

For a systematic analysis, as well as to understand how different layers and interfaces impact the excitation of different modes in a planar PNL with 2-D NHA, we calculate and present the dispersion relations for four cases: When the structure consists of (i) an infinite dielectric material and a finite metal layer, (ii) a finite dielectric material and a finite metal layer, (iii) a finite gain material and a finite metal layer, and (iv) a finite gain material and a finite metal layer with NHA. These cases represent the gradual evolution of the dispersion of the structure as we introduce an increasing degree of complexity to the structure with the fourth case approximating the nanolaser structure studied in this work.

In the first case, when the structure has an infinite dielectric material and a finite metal layer, we extend the PU layer thickness beyond the simulation region, as shown in Fig. 5(a), so that scattered light from the metal layer cannot couple to any photonic mode within the PU layer, rather gets absorbed by the PML layers at the boundary. The calculated dispersion relation for this structure is given in Fig. 5(b). We note two light lines in the dispersion diagram: The one with the greater slope corresponds to that in air and the other corresponds to that in PU layer. SPR occurs at ~550 THz. In the second case, the PU layer thickness is finite and smaller than the simulation region, as shown in Fig. 5(c), so that the scattered light from metal layer can couple to photonic modes within the PU layer. In this case, the PU layer has a thickness of 325 nm. The corresponding dispersion relation is given in Fig. 5(d). We note that there are several branches of available solutions between the two light lines, which represent several photonic modes being excited within the finite PU layer, especially, in the higher frequency or shorter wavelength range. However, the two light lines and the SPR frequency remain unchanged.

Now, we consider the case when the structure has a finite PU dielectric layer, which is doped with IR-140 dye molecules. In our 4-level 2-electron model, IR-140 has an absorption peak at 800 nm, or equivalently, at ~375 THz, and an emission or fluorescence peak at 870 nm, or equivalently, at ~345 THz. A schematic illustration along with the simulation domain for the calculation of dispersion relation of a structure that has a gain material and a finite metal layer is shown in Fig. 5(e). The corresponding dispersion relation in Fig. 5(f) shows two horizontal stripes: The upper stripe centered at ~375 THz is the absorption spectrum and the lower one centered at ~345 THz is the fluorescence spectrum of IR-140. The two profiles are nearly indistinguishable due to the broadband absorption and fluorescence profiles of IR-140 [19]. The fluorescence band signifies the fact that although a lot of modes can be excited in the structure, only the resonances that overlap with the fluorescence spectrum of IR-140 at ~345 THz can have gain, and hence, sustained oscillations. We note that the dispersion relations of the light lines, SPR, and photonic modes remain unchanged despite the inclusion of IR-140 dye molecules into the PU layer.

Finally, we analyze the dispersion relation of the structure that has a finite gain material and a metal layer with a periodic 2-D NHA. The schematic illustration of the structure with the simulation boundary and the corresponding dispersion relation are shown in Fig. 5(g) and (h), respectively. In this case, we carried out 3-D simulations to calculate the dispersion relation as well as to analyze the effects of NHA on the dispersion relation. We note that even with the presence of the 2-D NHA, the light lines, photonic modes, and SPR remain the same as were found for the third case without the 2-D NHA. This finding is corroborated by an earlier report [33], which indicates that the SPR branch of a hybrid hole-plasmon resonance is identical to that of a purely continuous metal layer. However, we note that the dispersion diagram in Fig. 5(h) is criss-crossed by a number of new lines, especially a few branches slanting from left to right. The appearance of these new dispersion lines can be explained via the momentum matching condition [34]

$$\vec{k}_x \pm i\vec{G}_x \pm j\vec{G}_y = \vec{k}_{sp} \tag{6}$$

where $\vec{k}_x = \vec{k}_0 \sin\theta_{inc}$ is the in-plane wavevector of light incident at an angle θ_{inc} with a wavevector $\vec{k}_0$, $\vec{G}_x$ and $\vec{G}_y$ are the reciprocal vectors associated with the periodicity of holes in the x- and y-directions, which are the same due to the symmetry of NHA distribution, and i and j are integers indicating the order of scattering from holes that couples incident light to a resonant mode $\vec{k}_{sp}$ of the structure. These new branches are the manifestation of Wood's anomaly [35]. They are observed when a surface wave, having been diffracted by the nanoholes, grazes the perforated plane instead of creating a plasmonic mode [34]. These dispersion lines can be analytically solved for by plugging $k_{sp} = 0$ in Eq. (6) [36].

In all cases, we note a vertical stripe around $k_x \approx 0$, which is consistent with the simulation results of Ref. [35]. The appearance of this vertical stripe stems from the use of Bloch BCs to simulate periodicity. Bloch BCs are different from normal periodic BCs. Periodic BCs simply make a copy of the fields from one boundary of the simulation region and paste it on to the other. Bloch BCs, on the other hand, apply a

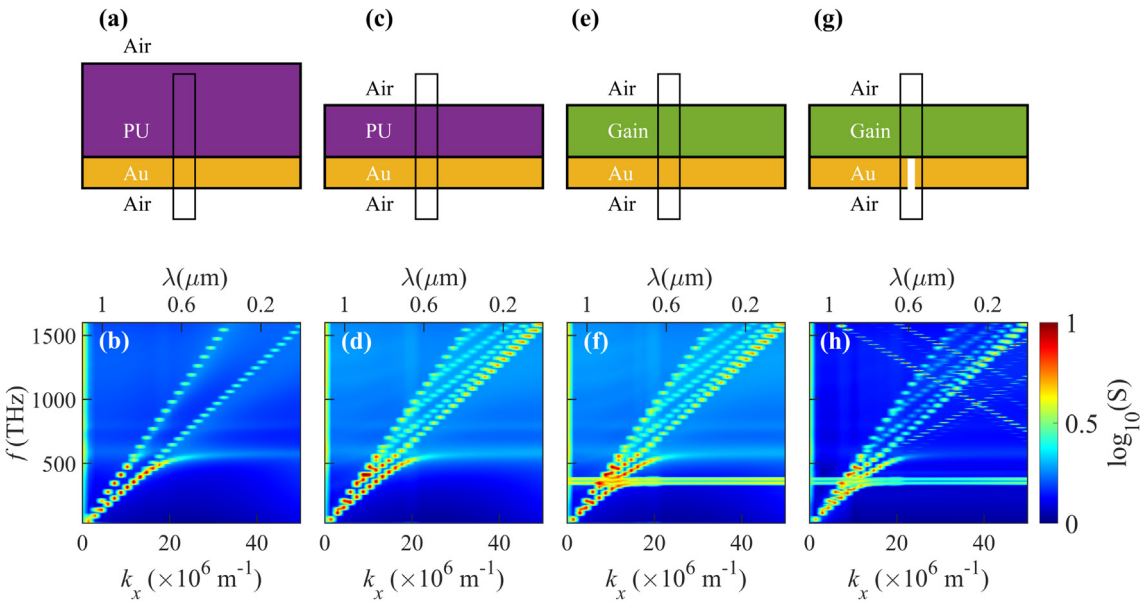

Fig. 5. Schematic illustration of the simulated structure with simulation domain and the corresponding dispersion relation for four cases: (a,b) An infinite dielectric material and a metal layer, (c,d) a finite dielectric material and a metal layer, (e,f) a finite gain material and a metal layer, and (g,h) a finite gain material and a metal layer with a 2-D NHA.

Table 3
Summary of the dispersion analysis results of the investigated cases.

Case	PU layer	Dye molecules	NHA	Photonic modes	SPR	Absorption and fluorescence	Wood's anomaly modes
1	Semi-infinite	No	No	No	Yes	No	No
2	Finite	No	No	Yes	Yes	No	No
3	Finite	Yes	No	Yes	Yes	Yes	No
4	Finite	Yes	Yes	Yes	Yes	Yes	Yes

phase shift of $k_x a_x$, where a_x is the periodicity of the Bloch unit cell, before replicating the fields to the opposite boundary. Depending on the value of k_x, some frequencies will destructively interfere, and therefore, will not appear in the dispersion diagram. However, for $k_x \approx 0$, the phase shift from the Bloch BCs will be small, and hence, they will be reduced to quasi-periodic BCs. This translates to the destructive interference effect not being as pronounced, and consequently, non-resonant frequencies will not vanish, resulting in a vertical band near $k_x \approx 0$. In Table 3, we summarize the key findings from the dispersion analysis of the four investigated cases.

4.2. Spectral decomposition

The gain lineshape of IR-140 dye molecules embedded within a PU host medium is presented in Fig. 6 as a dash-dotted red line. The typical values to determine α_m are taken from Table 2. The resultant curve, centered at $\lambda = 870$ nm, traces a lorentzian lineshape with a linewidth of ~100 nm. Furthermore, we employ the simulation strategy described in the methodology section in order to spectrally isolate the SPP mode. The result is shown in solid blue line in Fig. 6. We can identify two peaks in this Figure: a strong, coherent plasmonic mode at $\lambda = 865$ nm and a smaller, almost indistinguishable mode at $\lambda = 874$ nm. This dual peak stems from the use of gold in our structure which can sustain both transverse and longitudinal SPR [14]. The two peaks centered around $\lambda = 865$ nm and $\lambda = 874$ nm correspond to the transverse and longitudinal modes, respectively. The longitudinal SPR is patently insignificant in terms of its contribution to lasing action in this design. The transverse SPR mode is what facilitates lasing emission by coupling at the output. To gain a deeper understanding of what actually transpired, we can invoke the dispersion diagram in Fig. 5(d). As we can see, stimulated emission in the vicinity of the laser operating point excites SPPs, which in turn, function as nanoresonators, the *a priori* condition for lasing.

The output emission (dashed green line) is recorded at 1 μm away from the edge of the metal layer, on the far side of the device. We detect the emergence of a narrow peak around 875 nm. This is basically the EOT through the 2-D NHA that primarily contributes to the lasing emission in this design [37]. We note that the lasing spectra is red-shifted relative to the SPP mode, which can also be explained with recourse to the dispersion diagram. As SPR lies below the light line in the dispersion relation, plasmonic modes have higher wavevectors compared to free-space wavevectors. Hence, when SPP couples to the radiative mode via EOT, there is a dip in wavevector, or inversely, an increase in wavelength. Therefore, the lasing emission red-shifts from the SPP mode. Furthermore, we note a small bump around 790 nm. A fraction of the pump beam scatters forward through the DBR on the transmission side.

4.3. Tuning emission spectra

Ahmed et al. showed that the emission wavelength of the studied planar PNL can be tuned by changing the spacer TiO_2 layer thickness (d_l) and the incident angle (θ_{inc}) of the pump pulse [15]. While the emission wavelength red-shifts when d_l increases, the emission wavelength blue-shifts when θ_{inc} increases, which is contrary to what is expected from conventional lasers where lasing emission is created from resonating photonic cavity modes. Therefore, to understand the tuning mechanism of a planar PNL with a 2-D NHA, we investigate the excited modes and relate them with the output emission when d_l and θ_{inc} change.

Terminating TiO_2 layer thickness

The peak SPR wavelength λ_{peak} of a plasmonic structure is a function of the surrounding dielectric media [38]. As the effective dielectric constant of the ambient environment increases, red-shifting behavior of the SPP mode is observed [39,40]. The effective dielectric constant,

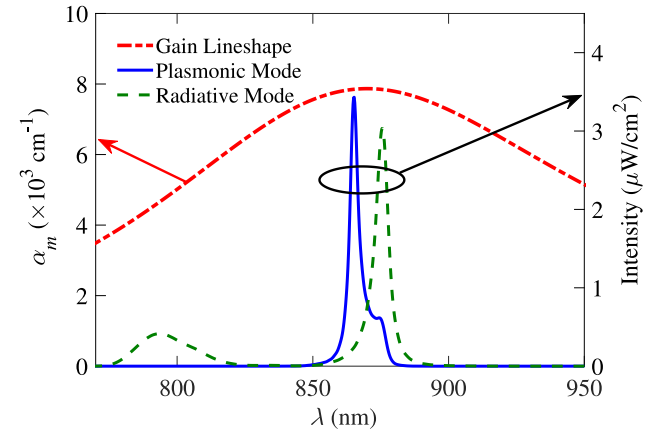

Fig. 6. The gain lineshape of IR-140 and the confined and emitted modal components of the studied PNL. The surface plasmon mode has been calculated at the metal-DBR interface and the radiative mode has been calculated at 1 μm away from the edge of the metal layer.

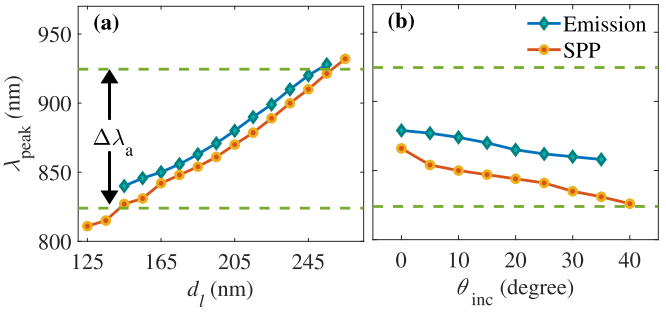

Fig. 7. The peak positions (λ_{peak}) of output emission and SPP modes as (a) spacer TiO_2 layer thickness (d_l) increases and (b) incident angle (θ_{inc}) increases.

in turn, is positively correlated with the thickness of the dielectric layer: The thicker the layer, the greater the dielectric constant. This phenomenon can be explained with recourse to the local field theory [41]. Therefore, theoretically speaking, if the thickness of the spacer TiO_2 layer increases, the SPP mode should red-shift and the lasing mode should follow suit, given that the lasing emission principally depends on the plasmonic mode.

This is exactly the pattern that emerges in Fig. 7(a) as the spacer layer thickness d_l increases. We find that λ_{peak} for the SPP mode increases from 824 nm to 921 nm, as d_l varies from 145 nm to 255 nm. Correspondingly, λ_{peak} for the lasing emission changes from 840 nm to 928 nm. However, the tunability range of λ_{peak} for the lasing emission is capped on both ends. No lasing is observed beyond either $d_l \lesssim 140$ nm or $d_l \gtrsim 260$ nm. The change of location of λ_{peak} of the SPP mode with respect to the gain lineshape explains the vanishing of the lasing emission. As d_l varies, the SPP mode eventually shifts away from the gain linewidth of IR-140 in both directions, which is shown by the dashed green line in Fig. 7(a). Hence, the gain medium can no longer compensate for the intrinsic loss of the PNL system and lasing emission ceases.

Incidence angle of the pump pulse

The resonant wavelength of plasmonic modes also changes when the incident angle of the pump pulse varies [16,42,43]. Zhou et al. demonstrated in their nanocavity array-based plasmonic laser that emission spectra blue-shifts from 913 nm to 850 nm when the incidence angle increases from 0 to 40° [44]. We explore the physics of the incidence angle-dependent tunability mechanism of the planar PNL design studied in this work.

We note that λ_{peak} of both the lasing emission and the SPP mode blue-shifts with the increase of θ_{inc}, as shown in Fig. 7(b). The λ_{peak} of SPP decreases from 866 nm to 831 nm as the incidence angle varies from 0 to 35°. Likewise, the lasing mode blue-shifts from 879 nm to 858 nm. Similar to the previous case, there is an upper limit for tunability. No lasing is observed beyond the critical angle $\theta_{inc} = 35°$ since the SPP mode strays too far from the peak of the gain emission of IR-140 dye molecules. The reason behind the blue-shifting of lasing emission can be qualitatively understood from the dispersion diagrams. As θ_{inc} increases, plasmonic resonance moves to a larger wavevector k_{sp}, as can be seen from Eq. (6). With increasing k_{sp}, plasmonic mode shifts to a lower λ_{peak}, and consequently, the lasing emission blueshifts too. We also note that the tunable range with the change in θ_{inc} is smaller than that obtained with the change in d_l.

We find that the SPP mode trails the lasing mode and always moves in lockstep with the lasing mode. A red- or blue-shift of the SPP mode produces a similar behavior for the lasing mode. This vital information presents us with a scientific strategy to tune the emission spectra of a PNL. Via this route, the emission spectra of PNLs can be tuned proactively over a broad range.

5. Conclusion

In this work, we identified the constitutive elements of a plasmon-mediated nanolaser. We isolated the SPP mode that emerges at the metal–dielectric interface and found that the SPP mode is definitively linked with the lasing emission in a planar PNL with 2-D metallic NHA. The calculated dispersion relations explain the excitation of SPP modes in the parallel plane PNL structure and the coupling between free-space and surface-bound modes. Our detailed analysis showed that the SPP mode is the critical determinant of lasing action of a planar PNL, which can be used as a tool to tune the emission spectra as well. Although this work deals with a planar PNL, similar behavior will evolve in nanowire- and nanoparticle-based PNL designs as plasmonic modes will play a more significant role in those designs.

Declaration of competing interest

The authors declare that they have no known competing financial interests or personal relationships that could have appeared to influence the work reported in this paper.

Funding

This research did not receive any specific grant from funding agencies in the public, commercial, or not-for-profit sectors.

References

[1] Ren-Min Ma, Rupert F. Oulton, Applications of nanolasers, Nature Nanotechnol. 14 (1) (2019) 12–22.
[2] Cun-Zheng Ning, Semiconductor nanolasers and the size-energy-efficiency challenge: a review, Adv. Photonics 1 (1) (2019) 014002.
[3] Chun Li, Zhen Liu, Jie Chen, Yan Gao, Meili Li, Qing Zhang, Semiconductor nanowire plasmonic lasers, Nanophotonics 8 (12) (2019) 2091–2110.
[4] Litu Xu, Fang Li, Yahui Liu, Fuqiang Yao, Shuai Liu, Surface plasmon nanolaser: Principle, structure, characteristics and applications, Appl. Sci. 9 (5) (2019) 861.
[5] Shaimaa I. Azzam, Alexander V. Kildishev, Ren-Min Ma, Cun-Zheng Ning, Rupert Oulton, Vladimir M. Shalaev, Mark I. Stockman, Jia-Lu Xu, Xiang Zhang, Ten years of spasers and plasmonic nanolasers, Light: Sci. Appl. 9 (1) (2020) 1–21.
[6] Stefan Alexander Maier, Plasmonics: Fundamentals and Applications, Springer Science & Business Media, 2007.
[7] Martin T. Hill, Yok-Siang Oei, Barry Smalbrugge, Youcai Zhu, Tjibbe De Vries, Peter J. Van Veldhoven, Frank W.M. Van Otten, Tom J. Eijkemans, Jaroslaw P. Turkiewicz, Huug De Waardt, et al., Lasing in metallic-coated nanocavities, Nature Photonics 1 (10) (2007) 589.
[8] Shao-Lei Wang, Suo Wang, Xing-Kun Man, Ren-Min Ma, Loss and gain in a plasmonic nanolaser, Nanophotonics 1 (ahead-of-print) (2020).
[9] Rupert F. Oulton, Volker J. Sorger, Thomas Zentgraf, Ren-Min Ma, Christopher Gladden, Lun Dai, Guy Bartal, Xiang Zhang, Plasmon lasers at deep subwavelength scale, Nature 461 (7264) (2009) 629.

[10] Kuankuan Ren, Jian Wang, Shaoqiang Chen, Qingxin Yang, Jiao Tian, Haichao Yu, Mingfei Sun, Xiaojun Zhu, Shizhong Yue, Yang Sun, et al., Realization of perovskite-nanowire-based plasmonic lasers capable of mode modulation, Laser Photonics Rev. 13 (7) (2019) 1800306.
[11] R.F. Oulton, G. Bartal, D.F.P. Pile, Xiang Zhang, Confinement and propagation characteristics of subwavelength plasmonic modes, New J. Phys. 10 (10) (2008) 105018.
[12] Chi Pang, Rang Li, Ziqi Li, Ningning Dong, Jun Wang, Feng Ren, Feng Chen, Plasmonic Ag nanoparticles embedded in lithium tantalate crystal for ultrafast laser generation, Nanotechnology 30 (33) (2019) 334001.
[13] Jie Yang, Zhengzheng Liu, Zhiping Hu, Fanju Zeng, Zeyu Zhang, Yao Yao, Zhiqiang Yao, Xiaosheng Tang, Juan Du, Zhigang Zang, et al., Enhanced single-mode lasers of all-inorganic perovskite nanocube by localized surface plasmonic effect from Au nanoparticles, J. Lumin. 208 (2019) 402–407.
[14] Xiangeng Meng, Alexander V. Kildishev, Koji Fujita, Katsuhisa Tanaka, Vladimir M. Shalaev, Wavelength-tunable spasing in the visible, Nano Lett. 13 (9) (2013) 4106–4112.
[15] Zabir Ahmed, Muhammad Anisuzzaman Talukder, An efficient and directional optical tamm state assisted plasmonic nanolaser with broad tuning range, J. Phys. Commun. 2 (4) (2018) 045016.
[16] M. Kaliteevski, I. Iorsh, S. Brand, R.A. Abram, J.M. Chamberlain, A.V. Kavokin, I.A. Shelykh, Tamm plasmon-polaritons: Possible electromagnetic states at the interface of a metal and a dielectric Bragg mirror, Phys. Rev. B 76 (16) (2007) 165415.
[17] Yang Mi, Bao Jin, Liyun Zhao, Jie Chen, Shuai Zhang, Jia Shi, Yangguang Zhong, Wenna Du, Jun Zhang, Qing Zhang, et al., High-quality hexagonal nonlayered CdS nanoplatelets for low-threshold whispering-gallery-mode lasing, Small 15 (35) (2019) 1901364.
[18] Qing Zhang, Son Tung Ha, Xinfeng Liu, Tze Chien Sum, Qihua Xiong, Room-temperature near-infrared high-Q perovskite whispering-gallery planar nanolasers, Nano Lett. 14 (10) (2014) 5995–6001.
[19] Jyotirmayee Mohanty, Dipakk Palit, J.P. Mittal, Photophysical properties of two infrared laser dyes–IR-144 and IR-140: A picosecond laser flash photolysis study, Proc.-Indian Natl. Sci. Acad. A 66 (2) (2000) 303–315.
[20] Maude Amyot-Bourgeois, Elham Karami Keshmarzi, Choloong Hahn, R. Niall Tait, Pierre Berini, Gain optimization, bleaching, and e-beam structuring of IR-140 doped PMMA and integration with plasmonic waveguides, Opt. Mater. Express 7 (11) (2017) 3963–3978.
[21] Babak Dastmalchi, Philippe Tassin, Thomas Koschny, Costas M. Soukoulis, A new perspective on plasmonics: confinement and propagation length of surface plasmons for different materials and geometries, Adv. Opt. Mater. 4 (1) (2016) 177–184.
[22] Aleksandr S. Baburin, Aleksey S. Kalmykov, Roman V. Kirtaev, Dmitriy V. Negrov, Dmitriy O. Moskalev, Ilya A. Ryzhikov, Pavel N. Melentiev, Ilya A. Rodionov, Victor I. Balykin, Toward a theoretically limited SPP propagation length above two hundred microns on an ultra-smooth silver surface, Opt. Mater. Express 8 (11) (2018) 3254–3261.
[23] Wei Ma, Zhaocheng Liu, Zhaxylyk A Kudyshev, Alexandra Boltasseva, Wenshan Cai, Yongmin Liu, Deep learning for the design of photonic structures, Nature Photonics (2020) 1–14.
[24] L.G. Nair, Dye lasers, Prog. Quantum Electron. 7 (3–4) (1982) 153–268.
[25] Shih-Hui Chang, Allen Taflove, Finite-difference time-domain model of lasing action in a four-level two-electron atomic system, Opt. Express 12 (16) (2004) 3827–3833.
[26] Anthony E. Siegman, A.E. Siegman, Lasers, Vol. 122, McGraw-Hill, New York, 1986, pp. 270–272.
[27] Carl M. Liebig, W.M. Dennis, Optical dephasing in saturable-absorbing organic dye IR140, Appl. Opt. 45 (9) (2006) 2072–2076.
[28] Jean-Pierre Bérenger, Perfectly matched layer (PML) for computational electromagnetics, Synth. Lect. Comput. Electromagn. 2 (1) (2007) 1–117.
[29] N. Sukumar, J.E. Pask, Classical and enriched finite element formulations for Bloch-periodic boundary conditions, Internat. J. Numer. Methods Engrg. 77 (8) (2009) 1121–1138.
[30] H. Sami Sözüer, Joseph W. Haus, Photonic bands: simple-cubic lattice, J. Opt. Soc. Amer. B 10 (2) (1993) 296–302.
[31] Glenn S. Smith, et al., A total-field/scattered-field plane-wave source for the FDTD analysis of layered media, IEEE Trans. Antennas and Propagation 56 (1) (2008) 158–169.
[32] Mike Potter, Jean-Pierre Bérenger, A review of the total field/scattered field technique for the FDTD method, FERMAT 19 (2017) 1–13.
[33] Tae-Ho Park, Joong-Wook Lee, Daniel M. Mittleman, Peter Nordlander, Polarization dependent terahertz spectroscopy of a single subwavelength hole in thin metallic film, in: Plasmonics: Metallic Nanostructures and their Optical Properties VII, Vol. 7394, International Society for Optics and Photonics, 2009, p. 73940F.
[34] H.F. Ghaemi, Tineke Thio, Deeal Grupp, Thomas W. Ebbesen, H.J. Lezec, Surface plasmons enhance optical transmission through subwavelength holes, Phys. Rev. B 58 (11) (1998) 6779.
[35] William L. Barnes, W. Andrew Murray, J. Dintinger, E. Devaux, T.W. Ebbesen, Surface plasmon polaritons and their role in the enhanced transmission of light through periodic arrays of subwavelength holes in a metal film, Phys. Rev. Lett. 92 (10) (2004) 107401.
[36] Mikhail M. Voronov, Resonant wood's anomaly diffraction condition in dielectric and plasmonic grating structures, 2016, arXiv preprint arXiv:1612.08674.
[37] K.L. Van der Molen, K.J. Klein Koerkamp, Stefan Enoch, Franciscus B. Segerink, N.F. Van Hulst, L. Kuipers, Role of shape and localized resonances in extraordinary transmission through periodic arrays of subwavelength holes: Experiment and theory, Phys. Rev. B 72 (4) (2005) 045421.
[38] G. Xu, M. Tazawa, P. Jin, S. Nakao, K. Yoshimura, Wavelength tuning of surface plasmon resonance using dielectric layers on silver island films, Appl. Phys. Lett. 82 (22) (2003) 3811–3813.
[39] G. Xu, M. Tazawa, P. Jin, S. Nakao, Surface plasmon resonance of sputtered ag films: substrate and mass thickness dependence, Appl. Phys. A 80 (7) (2005) 1535–1540.
[40] Gang Xu, Chun-Ming Huang, Qing Liang, Masato Tazawa, Ping Jin, Wavelength multiplexing and tuning in nano-ag/dielectric multilayers, Appl. Phys. A 94 (3) (2009) 525–530.
[41] Kenji Natori, Daijiro Otani, Nobuyuki Sano, Thickness dependence of the effective dielectric constant in a thin film capacitor, Appl. Phys. Lett. 73 (5) (1998) 632–634.
[42] Ying-Shin Huang, Sheng-Yao Hu, Chia-Chih Huang, Yueh-Chien Lee, Jyh-Wei Lee, Chung-Cheng Chang, Zin-Kuan Wun, Kwong-Kau Tiong, Incident-angle-dependent reflectance in distributed bragg reflectors fabricated from ZnO/MgO multilayer films, Opt. Rev. 21 (5) (2014) 651–654.
[43] A.V. Kavokin, I.A. Shelykh, G. Malpuech, Lossless interface modes at the boundary between two periodic dielectric structures, Phys. Rev. B 72 (23) (2005) 233102.
[44] Wei Zhou, Montacer Dridi, Jae Yong Suh, Chul Hoon Kim, Dick T. Co, Michael R. Wasielewski, George C. Schatz, Teri W. Odom, et al., Lasing action in strongly coupled plasmonic nanocavity arrays, Nature Nanotechnol. 8 (7) (2013) 506.